The Astrophysical Journal, 652:426–441, 2006 November 20

INFRARED OBSERVATIONS OF THE HELIX PLANETARY NEBULA

Joseph L. Hora,[1] William B. Latter,[2] Howard A. Smith,[1] and Massimo Marengo[1]
Received 2006 May 10; accepted 2006 July 20

ABSTRACT

We have mapped the Helix (NGC 7293) planetary nebula (PN) with the IRAC instrument on the *Spitzer Space Telescope*. The Helix is one of the closest bright PNs and therefore provides an opportunity to resolve the small-scale structure in the nebula. The emission from this PN in the 5.8 and 8 μm IRAC bands is dominated by the pure rotational lines of molecular hydrogen, with a smaller contribution from forbidden line emission such as [Ar III] in the ionized region. The IRAC images resolve the "cometary knots," which have been previously studied in this PN. The "tails" of the knots and the radial rays extending into the outer regions of the PN are seen in emission in the IRAC bands. IRS spectra on the main ring and the emission in the IRAC bands are consistent with shock-excited H_2 models, with a small ($\sim$10%) component from photodissociation regions. In the northeast arc, the H_2 emission is located in a shell outside the Hα emission.

Subject headings: planetary nebulae: general — planetary nebulae: individual (Helix Nebula, NGC 7293)

1. INTRODUCTION

One of the remarkable features of the Helix (NGC 7293, PN G036.1−57.1) planetary nebula (PN) is the small-scale structure in its expanding shells. The appearance is more striking because of the close proximity (213 pc; Harris et al. 1997) of the Helix compared to other PNs, giving us a clearer view of the nebula's structure. The distribution of material in the Helix is unlike the simple classical picture of a uniform spherical shell expanding isotropically from the central star. Instead, the material in the shells is seen to reside in cometary knots and clumps, and the structure of these clumps changes as a function of distance from the central star. O'Dell et al. (2004) combined *Hubble Space Telescope* (*HST*) and ground-based imaging to provide a comprehensive picture of the Helix. Closest to the central star are the cometary knots, which have highly ionized emission along their rims nearest the central star and fainter emission along the edges of the material that is trailing away from the star. Farther from the central star are the main rings of the nebula, in which the knots are closely spaced and not as sharply defined as the inner cometary knots. Outside the main rings, faint rays of emission extend out to a diffuse outermost ring at a radius approximately 15′ from the central star. O'Dell et al. (2004) conclude that the nebular structure consists of an inner disk roughly in the plane of the sky, surrounded by a highly inclined torus, with an outer ring at roughly twice the diameter of the inner structures.

The orientation of the Helix provides an excellent view of the region around the central star that has been cleared of molecular material and allows us to view the cometary knots nearly in profile. The cometary knots have been studied extensively, more recently with *HST* imaging and spectra providing the best resolution of the structures (e.g., Meaburn et al. 1992; O'Dell & Handron 1996; O'Dell & Burkert 1997; O'Dell et al. 2005; Meixner et al. 2005). The knots typically have a bright cusp of emission in Hα and forbidden lines such as [O I] and [N II]. In [O III] the knots and their tails are visible as shadows in the extended emission around the knot. In the 2.12 μm H_2 line, the emission is also brightest along the rim facing the central star (Huggins et al. 1992; Meixner et al. 2005), but there is significant emission from the tail in H_2 and CO. The structure and kinematics of the knots and their change in morphology from the inner to outer regions are consistent with the knots forming near the ionization front and being shaped by the stellar radiation as the ionization front moves outward (O'Dell et al. 2004). However, models of the H_2 emission from the knots (O'Dell et al. 2005; Meixner et al. 2005) fail to accurately reproduce the flux observed in the near-IR lines.

The ISOCAM instrument on board the *Infrared Space Observatory* (*ISO*) was used to produced infrared images and spectra of the Helix in the 5–17 μm spectral region (Cox et al. 1998). The nebula was mapped with 6″ resolution and millijansky sensitivity, and they found that the emission was dominated by the pure rotational lines of H_2 in the 5–12 μm region and by the 12.81 μm [Ne II] and 15.55 μm [Ne III] lines at longer wavelengths. Conspicuously absent was any emission from polycyclic aromatic hydrocarbons (PAHs), which one might expect from what they assumed was a carbon-rich nebula.

In this paper, we report results based on observations of the Helix PN using the Infrared Array Camera (IRAC; Fazio et al. 2004) and the Infrared Spectrograph (IRS; Houck et al. 2004) on board the *Spitzer Space Telescope* (Werner et al. 2004). With its higher resolution ($\sim$2″) and sensitivity (5 σ extended source sensitivity at 8 μm of 0.2 MJy sr^{-1} in 180 s) and wider field (5.′2 × 5.′2) than previous cameras in this wavelength range, IRAC is a powerful instrument for investigating nebular emission from gas and dust in PNs, reflection nebulae, and star-forming regions. The four IRAC channels sample the wavelength range from $\sim$3.1 to $\sim$9.5 μm, which potentially includes emission lines from ionized gas such as Brα at 4.05 μm, forbidden line emission such as the [Mg V] 5.6 μm, [Ne VI] 7.64 μm, and [Ar III] 8.99 μm lines, emission from H_2 from transitions in all four bands, CO emission from transitions near 4.65 μm, broad features such as the PAH lines at 3.3, 6.2, 7.7, and 8.6 μm, and continuum emission from warm or hot dust. Before *ISO* and *Spitzer*, previous observations of PNs in this wavelength range that were obtained from the ground were primarily of young objects, e.g., NGC 7027 (Aitken & Roche 1983) and BD +30 3639 (Hora et al. 1993), that were strong mid-IR sources due to their PAH or warm

[1] Harvard-Smithsonian Center for Astrophysics, 60 Garden Street, MS 65, Cambridge, MA 02138-1516.
[2] NASA Herschel Science Center, California Institute of Technology, MS 220-6, Pasadena, CA 91125.

dust emission. With IRAC, the mid-IR emission from more evolved PNs can be investigated. We are conducting a program to observe a sample of 35 PNs with IRAC. Initial results were reported in Hora et al. (2004a, 2005) and showed that IRAC was especially sensitive to the ionized gas emission in the nebulae and could detect faint H_2 emission in the outer shells and halos. In this paper we show the results for the Helix, which is the PN with the largest angular extent in the sample.

2. OBSERVATIONS AND DATA REDUCTION

2.1. *IRAC Images*

The observations were obtained with the IRAC instrument (Fazio et al. 2004) on the *Spitzer Space Telescope* (Werner et al. 2004). The 30 s high dynamic range (HDR) mode was used (AOR 0004422400). The HDR mode takes pairs of images with 1.2 and 30 s frame times (1.0 and 26.8 s exposure time) at each dither position in the IRAC channels 1–4 (3.6, 4.5, 5.8, and 8 μm; see Fazio et al. [2004] for the band transmissions and isophotal wavelengths). A 5×5 map was performed with six dither positions per map position, resulting in a median exposure time of $\sim$160 s. The S11.4.0 version of the Basic Calibrated Data (BCD) products from the *Spitzer* Science Center (SSC) pipeline were used to construct the mosaic images. The BCD products have the main instrumental signatures removed from the data and are calibrated in units of MJy sr^{-1}, based on the calibration derived from measurements of standard stars (Fazio et al. 2004; Reach et al. 2005). Some bright source residual artifacts in the pipeline images (Hora et al. 2004b) caused by bright stars were removed by forcing the column or row median in regions with no sources to be equal to that of adjacent columns or rows. Then the individual BCD images were combined into a single image for each channel and frame time using the SSC MOPEX mosaicker program. The IRAC_proc version 3.0 scripts developed by Schuster et al. (2006) were used to determine the pixel masks and run the MOPEX software. The output images were written with a linear pixel size $\frac{1}{3}$ that of the input pixels ($\frac{1}{9}$ of the area). For flux calibration, it was assumed that the zero-magnitude fluxes in the IRAC bands are 277.5. 179.5, 116.6, and 63.1 Jy for channels 1–4, respectively. A flux correction for the extended source emission was applied to the extracted fluxes used in this paper, as described in the *Spitzer* Observer's Manual[3] and Reach et al. (2005). For the extended emission fluxes presented here, the MJy sr^{-1} values in the images from the pipeline were multiplied by factors of 0.944, 0.937, 0.772, and 0.737 for IRAC channels 1–4, respectively. The local sky background in each IRAC band was estimated from regions outside the nebula and subtracted from the image.

2.2. *Ground-based Near-IR Molecular Hydrogen Image*

A narrowband near-IR image at 2.12 μm was obtained on 1997 June 18 using the QUIRC camera (Hodapp et al. 1996) and the Quick Infrared Survey Telescope (QUIST) on Mauna Kea. QUIST is a f/10 Ritchey-Chretien Cassegrain telescope with a 25.4 cm diameter primary that was attached to the top of QUIRC, and the system was mounted on the University of Hawaii (UH) 61 cm telescope on Mauna Kea for pointing. The observing for this project was controlled remotely from Kaneohe, HI, with the assistance of the UH 2.2 m telescope operator to open and close the dome and refill the camera's LN_2 supply. The QUIST telescope with QUIRC provided a pixel scale of $1\farcs68$ pixel^{-1} and a field of view of approximately $29' \times 29'$. A five-position dither pattern of 120 s frames was used that placed the nebula in the center of each quadrant and the center of the array, covering a roughly 1 deg^2 area. A total of 48 frames were obtained and mosaicked to form the final image. The QUIRC narrowband H_2 filter is roughly Gaussian in shape, centered at 2.124 μm with a bandwidth of 0.022 μm.

2.3. *IRS Spectra*

The spectra are from a calibration data set (AOR 0013736192) obtained on 2005 May 29 with the IRS. The low-resolution spectra used a ramp duration of 60 s with two cycles. Two positions were obtained on the main ring of the nebula and one position roughly $6'$ north of the ring. The S12.0.2 version of the BCD were used in the reduction. The data at each of the positions were averaged separately. Then the northern position spectral image was subtracted from the ring positions before they were extracted to remove the background, which is dominated by the zodiacal emission. The SPICE software (ver. v1.1-beta16) from the SSC was used to extract the spectra, using the full slit width. The IRS calibration is based on observations of point sources, so a slit loss correction factor was applied to normalize the spectra (Kelley et al. 2005). This correction should provide for accurate line ratios, but it may slightly affect the absolute calibration of the spectrum. The line fluxes were measured using the spectral analysis routines in the SMART version 5.5 IDL package written by the IRS team, which can be downloaded from the SSC Web site.

3. RESULTS

3.1. *IRAC Images*

The IRAC images of the Helix are shown in Figures 1–4. Figure 1 is a color image of three of the IRAC bands, as described in the figure legend. Figure 2 shows the core region to better display the structure of the cometary knots. Gray-scale images of the individual IRAC bands are shown in Figure 3, and the inner $6'$ are shown in Figure 4.

One of the most striking features of the color images is the cometary knots in the inner part of the nebula. In the optical images of the cometary knots as shown, for example, in O'Dell et al. (2005), the knots show a bright rim or cusp, and a shadowed region appears behind it. The brightest part of the knot is the surface that faces the central star. The tail is outlined in faint emission and appears limb-brightened, so the outer edges are brighter than the center of the tail. In the IRAC images, the tips of the knots are brighter in the 3.6 and 4.5 μm bands. In the 5.8 and 8 μm bands, the emission appears relatively constant along the knot, with little or no brightening at the tip. This is apparent in the color images of Figures 1 and 2, where the knots have blue-green tips and relatively redder tails.

Another feature of the images is that the emission in the IRAC bands is fragmented or clumpy throughout the nebula. The characteristics of the clumps vary in a systematic way as a function of radius in the nebula. In the inner portion there are isolated cometary knots with long tails. The heads of the knots are not resolved in the IRAC images. In the inner and outer rings, there are also small clumps of emission but with little or no tails seen. Beyond the outer ring, there are rays of emission that extend to the outermost ring. Also in this region are faint wisps of emission many arcseconds across that appear like bow shock regions but that are much larger than the cometary knots in the inner regions. The clumpy structure in the rings is consistent with that seen by Speck et al. (2002) and Meixner et al. (2005) in their H_2 images of the Helix.

[3] Available at http://ssc.spitzer.caltech.edu/documents/som/.

FIG. 1.—Three-color image of the Helix, showing the regions that were imaged in all IRAC bands. The 3.6, 4.5, and 8 μm IRAC bands are mapped to blue, green, and red, respectively. The orientation of the mosaic is in array coordinates, and the vertical axis is 59°.6 east of north (see Fig. 3). The image is approximately $24'.2 \times 26'.2$ in size.

3.1.1. *IRAC Fluxes and Colors of the Nebula*

Table 1 lists the fluxes and magnitudes of the main rings of the nebula. The halo region was not included, since not enough area was imaged in any of the bands to cover the entire halo. We restricted the flux calculation to an elliptical region around the nebula with major and minor axes of 1185″ and 822″, with the major axis oriented 60° west of north to align it with the longest dimension of the main rings. The bright stars 2MASS J22290943−2046073, 2MASS J22292575−2056519, and 2MASS J22292663−2057075 (*K* of 7.5–9.5), which are in the outer parts of the ring, were masked out from the flux total. The contribution from field stars was estimated by measuring the total flux from stars in an area outside the halo in each of the IRAC bands, normalizing it to the area of the nebula, and subtracting that from the total flux measured inside the ellipse.

The IRAC colors of the nebular emission are plotted in Figure 5. To make this plot, the IRAC images were binned to $2'' \times 2''$ pixels, and only pixels in which the 4.5 μm band surface brightness was greater than 0.09 MJy sr^{-1} were included in the calculation. Regions affected by the brightest stars were also masked, and the region inside the cometary knots was excluded. The color of the IRAC emission at each point was then calculated and plotted in groups of increasing radius bins. The

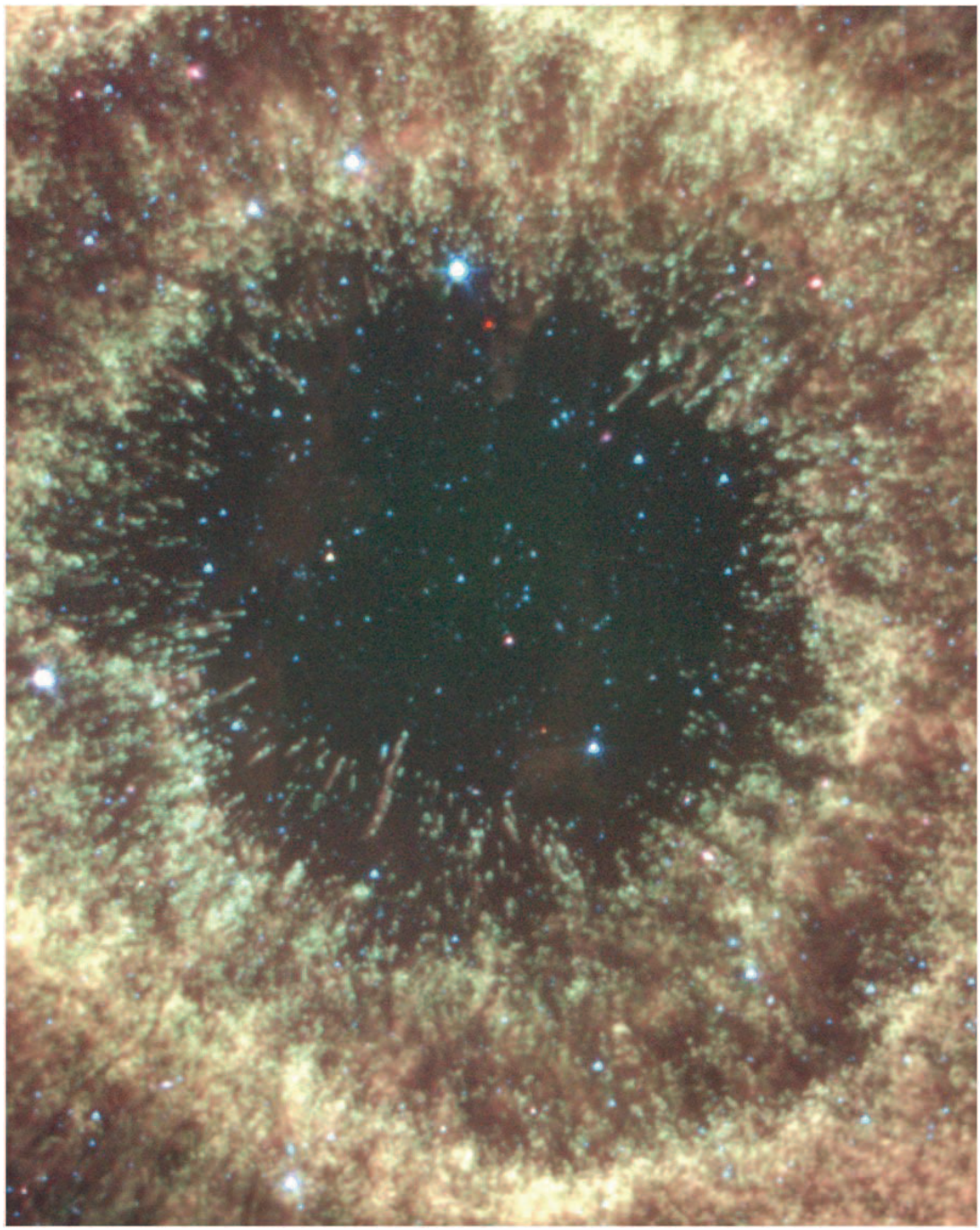

FIG. 2.—Same as in Fig. 1, except showing the $12' \times 11'$ region around the central star. This shows the structure of the knots inside the main nebular ring.

first bin includes the region inside the first ring, including the cometary knots. The second bin (*cyan dots*) contains the first ring, the third bin (*blue dots*) contains the second ring, and the last bin (*red dots*) includes the region exterior to the second ring, out to the limit of the detected emission but not including the halo or arcs outside the outer ring. No attempt was made to remove the background stars and galaxies that are visible in the images; they are contributing to the scatter of points in the diagram but are relatively small in number and uniformly distributed in the images, so they should not affect the relative colors of the regions in the nebula.

One can immediately see that the IRAC colors become redder in $[4.5] - [8]$ as a function of increasing radius. There is very little change in the $[3.6] - [4.5]$ color over the same range. The tips of the cometary knots are the extreme of the color range, with a median $[4.5] - [8]$ color of 1.1, compared to the rest of the nebula with medians that range from $\sim$2 to 2.5. The $[5.8] - [8]$ colors do not show this same trend. The regions outside $100''$ from the center have the same color, with a median value of 1.17. The inner $100''$ is slightly redder, with a median value of 1.3.

3.1.2. *Comparison with NICMOS and Other Data*

Figure 6 shows a comparison between a Near-Infrared Camera and Multi-Object Spectrometer (NICMOS) image in the ring (Meixner et al. 2005) and the same region from the IRAC

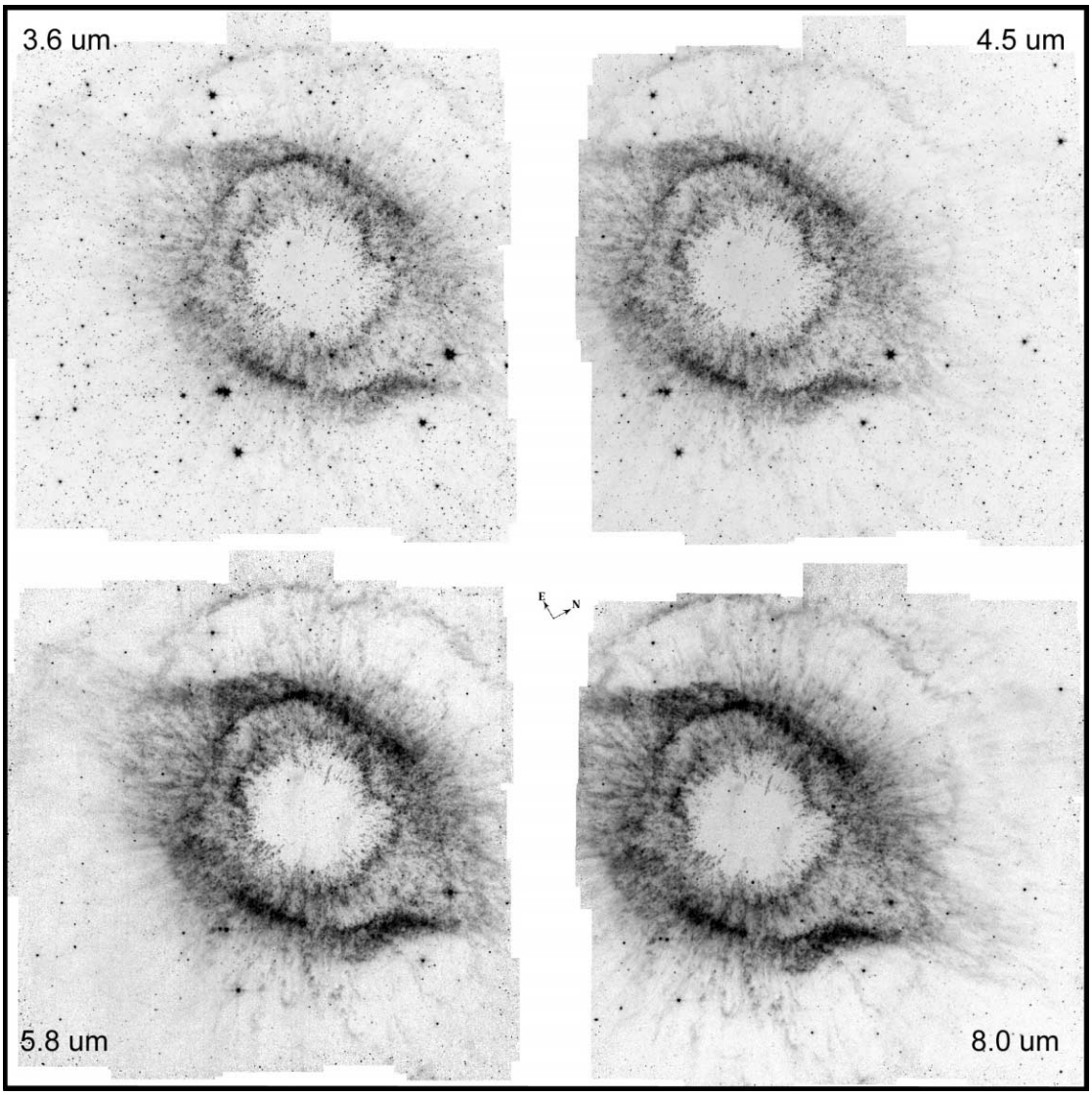

FIG. 3.—Gray-scale images of each of the individual IRAC bands. The images are labeled with the names of the IRAC bands, and the orientation is indicated by the arrows in the center of the image. The length of the arrows is 1′. The orientation of all the bands is the same, and each image is aligned vertically and horizontally with its neighbors.

4.5 μm image. Except for the better resolution of the NICMOS image, the images are very similar, with each feature in the NICMOS image matching a feature in the IRAC image and at approximately the same relative intensity. There are a few features in the IRAC image that appear different and are probably background stars or galaxies. These are brighter in the IRAC images due to the broader bandpass of the IRAC filters compared to the narrowband H_2 filter used for the NICMOS image, and the extragalactic sources are also relatively brighter at the longer wavelength of the IRAC image.

The close correspondence between the NICMOS and the IRAC data also implies that the IRAC emission is primarily from H_2 lines in the IRAC bands. The overall appearance of the nebula in the 2.12 μm H_2 line in the image presented here and by Speck et al. (2002) also demonstrates the correspondence between the near-IR and IRAC images of the nebula. Near-IR imaging of a cometary knot by Huggins et al. (2002) shows the H_2 emission concentrated at the face of the globule toward the central star, similar to the appearance in the 4.5 μm image. The IRS spectra presented here confirm that there are no other significant contributors to the IRAC band flux in the locations sampled.

There are, however, variations in the relative intensity of the IRAC images across the nebula. This is due to either changes in the relative line strengths of the H_2 emission in the IRAC bands or other minor components of the emission. One example is the [Ar III] line at 8.99 μm, which is detected in the *ISO* and IRS spectra and could contribute to the emission seen in the 8 μm image. In the IRS spectra here, the H_2 lines in the 8 μm band contribute approximately 25 times the flux from the [Ar III] line. For the IRAC 4.5 μm image, one possible contributor is the Brα emission line at 4.05 μm. We could find no published narrowband images of the Helix in this line. Speck et al. (2002) imaged the nebula in the 2.16 μm Brγ line of H I and do not detect any emission to the upper limit of 7×10^{-8} ergs s^{-1} cm^{-2} sr^{-1}. The Brα/Brγ line ratio would vary with extinction; observed ratios can range from $\sim$2.8 to 12 (e.g., Bunn et al. 1995). For a typical cometary knot, the peak surface brightness observed at the inner edge of the knot is approximately 0.5 MJy sr^{-1}, with a 1 σ noise

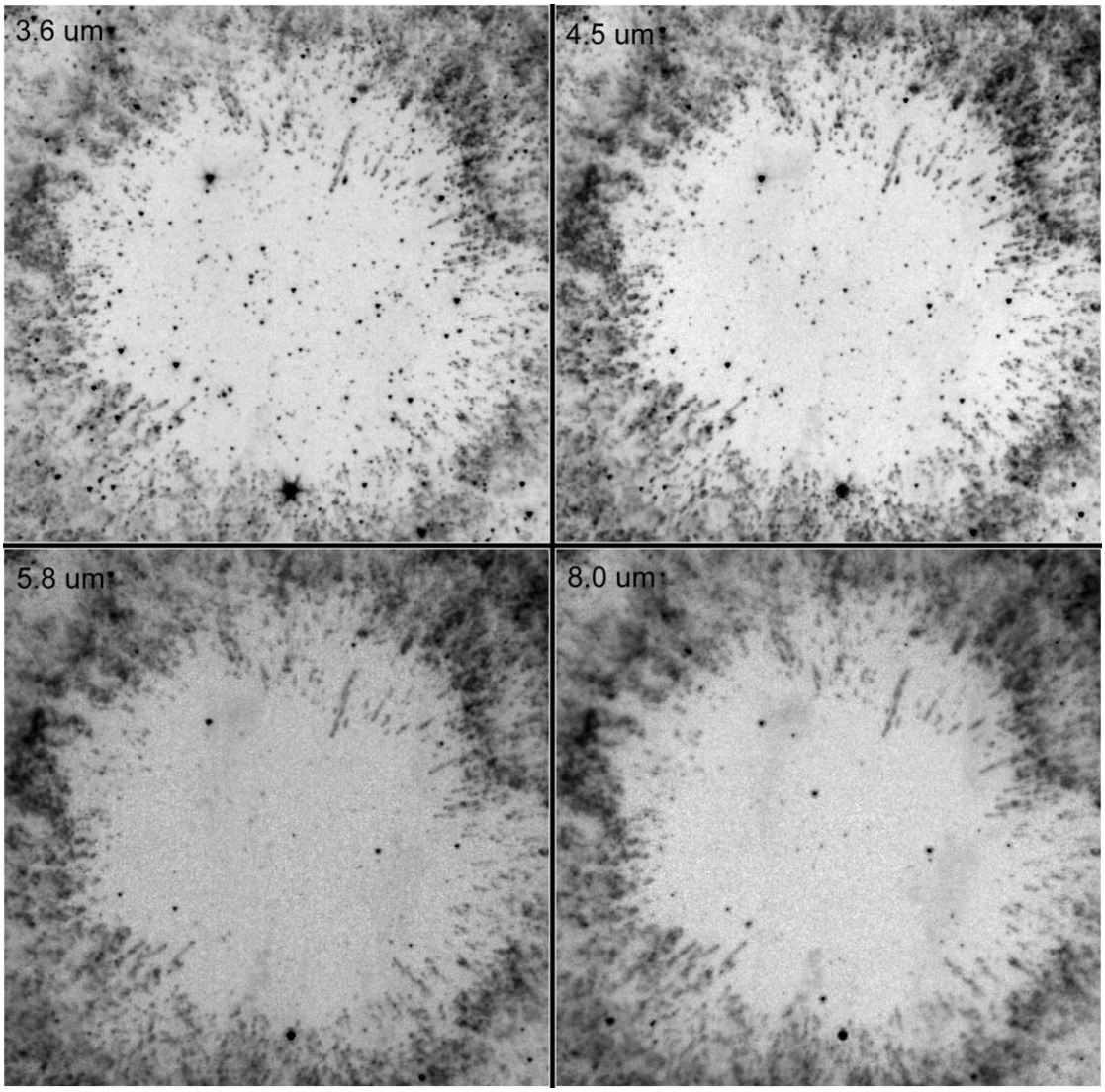

FIG. 4.—Same as Fig. 3, except just the inner $6' \times 6'$ region.

of 0.007 MJy sr^{-1}. If the Brα/Brγ ratio was greater than 12 in the Helix, it would be approximately 1% of the 4.5 μm band flux. Therefore, the contribution from the Brα line is unlikely to be significant in the knots.

Figure 7 illustrates the relationship between the emission detected by IRAC and the Hα emission. The IRAC 8 μm, IRAC 4.5 μm, and Advanced Camera for Surveys (ACS) F658N (Hα + [N II]) images are plotted as red, green, and blue, respectively, in this color image. The ACS image has been smoothed to match the IRAC 4.5 μm resolution. The image highlights the major differences between the Hα and IRAC emission. In the inner region, the cometary knots are brightest in Hα at the tips. Some tips are decidedly bluer, others appear a little green, perhaps due to extinction that affects the Hα to a greater degree. In the main ring, the emission differs drastically: the Hα emission is mostly smooth and seems to fill the whole region fairly uniformly, whereas the IRAC emission is very clumpy.

TABLE 1
IRAC FLUXES AND COLORS OF THE MAIN RINGS

IRAC Band (μm)	Flux (Jy)	Magnitude
3.6	1.71	5.54
4.5	3.35	4.32
5.8	6.07	3.19
8	9.66	2.06

3.2. *The* 2.12 μm H_2 *Image*

The 2.12 μm H_2 image obtained from Mauna Kea is shown in Figure 8. The image has lower spatial resolution and is not as deep as the IRAC images, but the overall structure of the 2.12 μm H_2 line is very similar to the emission in the IRAC images. The image is similar to the H_2 image of Speck et al. (2002). Here we have imaged a larger area and detect the faint radial rays extending from the ring to the outer shell. The northeast arc is also detected. Due to the lower resolution, it is more difficult to see the individual cometary knots, although the bright and better separated cometary knot 428-900 (O'Dell & Burkert 1997) and associated knots are visible.

3.3. *IRS Spectra*

Figure 9 shows the IRS spectra from the two locations indicated in Figure 10. The two locations are at approximately the same radial distance and both in the main rings, so as one might

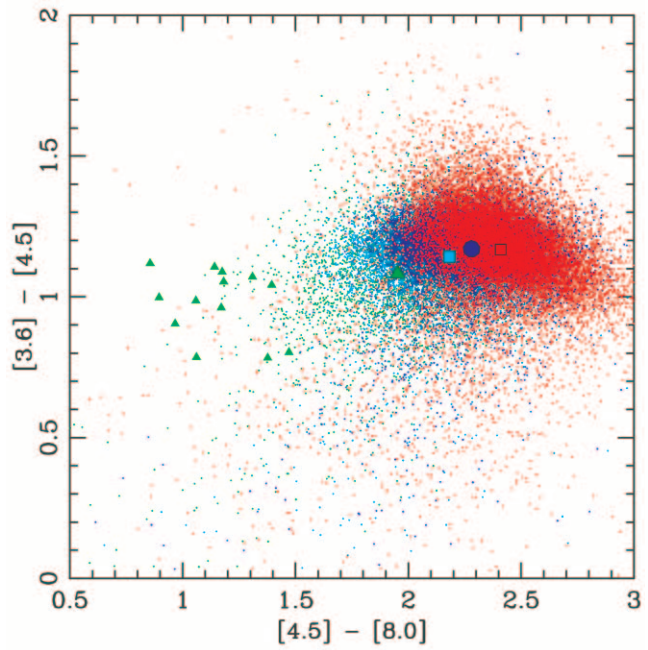

FIG. 5.—IRAC [3.6] − [4.5] vs. [4.5] − [8] color of the nebula. The small dots are the binned (2″ × 2″) pixels above the minimum flux cutoff. The green dots are those in the inner 200″, cyan are 220″–300″, blue are 320″–400″, and red are >400″ from the center of the nebula. Larger green, cyan, blue, and red symbols show the median of the distribution for the radius range. Smaller green filled triangles that appear left of center are the colors of the tips of isolated cometary knots, showing that they are much brighter in the 4.5 μm band than the rest of the nebula.

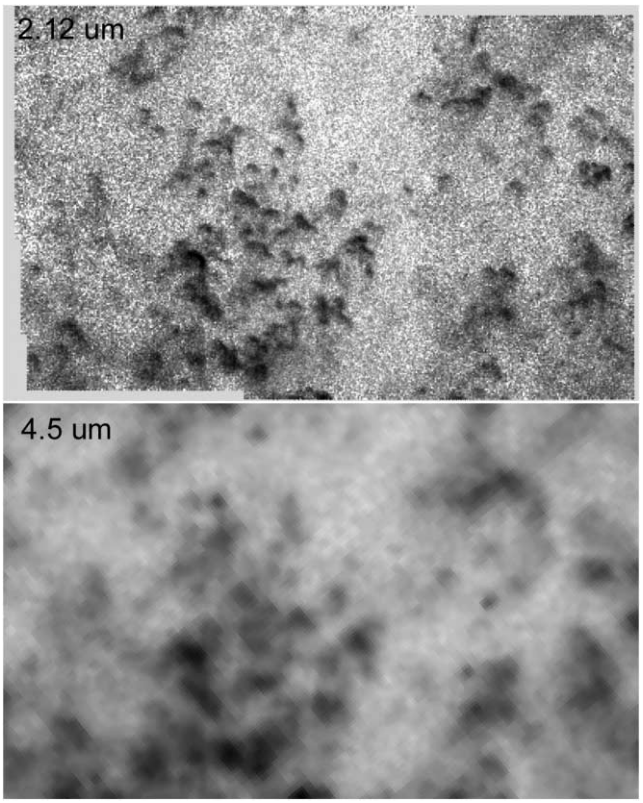

FIG. 6.—*Top:* NICMOS 2.12 μm H_2 image (Meixner et al. 2005, "position 2"). The total field is approximately 80″ × 50″, and north is 21°.89 clockwise from vertical. *Bottom:* Same area of the IRAC 4.5 μm image.

expect the observed spectra are very similar. The IRS data used for the background subtraction can be seen in Figure 10 to fall across the faint outer arc, which may slightly affect the spectra in Figure 9. However, assuming the emission in the arc is due to H_2, it is a factor of 10 lower than the emission in the ring, so it has little effect on the line fluxes measured for the two ring positions.

The dominant emission features from the nebula in this wavelength range are from the pure rotational lines of molecular hydrogen. The measured line fluxes are given in Table 2. These results are similar to what was found by Cox et al. (1998), who found that the emission from 5 to 16.6 μm was dominated by H_2 line emission, with a small contribution from the [Ar III] 8.99 μm and [Ne II] 12.81 μm lines. They found the [Ne III] 15.55 μm line to be strong, but the forbidden Ne lines are outside the IRAC wavelength range. Therefore, the emission in the IRAC 5.8 and 8 μm bands is primary from the $S(3)$ to $S(7)$ lines of H_2. The IRS spectra do not sample the 3.1–5.2 μm range of IRAC bands 1 and 2, so we do not have a direct measurement of the emission components. However, there are H_2 lines present throughout the 3–5 μm range (e.g., Black & van Dishoeck 1987), which are expected to be a major component of the emission in bands 1 and 2 (see § 4.2).

We compared the emission line flux in the IRS spectra to the IRAC flux densities in bands 3 and 4. Using the IRAC transmission curves (Fazio et al. 2004), the expected flux densities at positions 1 and 2 were determined based on the measured IRS spectra and are given in Table 3. The comparable IRAC flux was estimated by summing the emission in a 3.″6 × 57″ box centered at the IRS slit position. The IRS fluxes are slightly lower than the observed IRAC fluxes, but given the uncertainties in the extended source calibration and the way the fluxes were estimated, the measurements are consistent. The ratios between the two bands at each position are similar between the IRS and IRAC measurements, indicating that the line ratios in the IRS spectra are reasonably accurate.

Absent from the spectrum is any trace of PAH emission. Cohen & Barlow (2005) showed that the 7.7 μm PAH feature is seen in PNs with nebular C/O ratios greater than 0.6. Henry et al. (1999) determined that the Helix had an average nebular C/O ratio of 0.87; therefore, one would expect PAH emission. Cox et al. (1998) argue that the nebula is carbon-rich, since (1) molecular species such as CN, HCN, HNC, and HCO^+ are comparable with the abundances measured in carbon-rich nebulae, and (2) a high abundance of neutral carbon measured near the western rim is only expected in carbon-rich environments. The lack of detected PAH emission could be a sensitivity effect, since the nebula is very extended and the slit takes in a small fraction of the nebula, compared to other measurements in which most or all of the nebula is sampled by the spectrograph beam. Cohen & Barlow (2005) note that this may be the case for two PNs with large spatial extent in which they did not detect PAHs, but they also note that the nebulae may be optically thin to ionizing radiation and that no photodissociation regions (PDRs) exist in the PNs.

4. H_2 LINE EMISSION

4.1. *Modeling the* H_2 *Emission Observed at the IRS Positions*

We modeled the H_2 line emission using the calculations of Michael Kaufman and Mark Wolfire for shocks and PDRs (Kaufman et al. 2005, 2006; Kaufman & Neufeld 1996; Wolfire

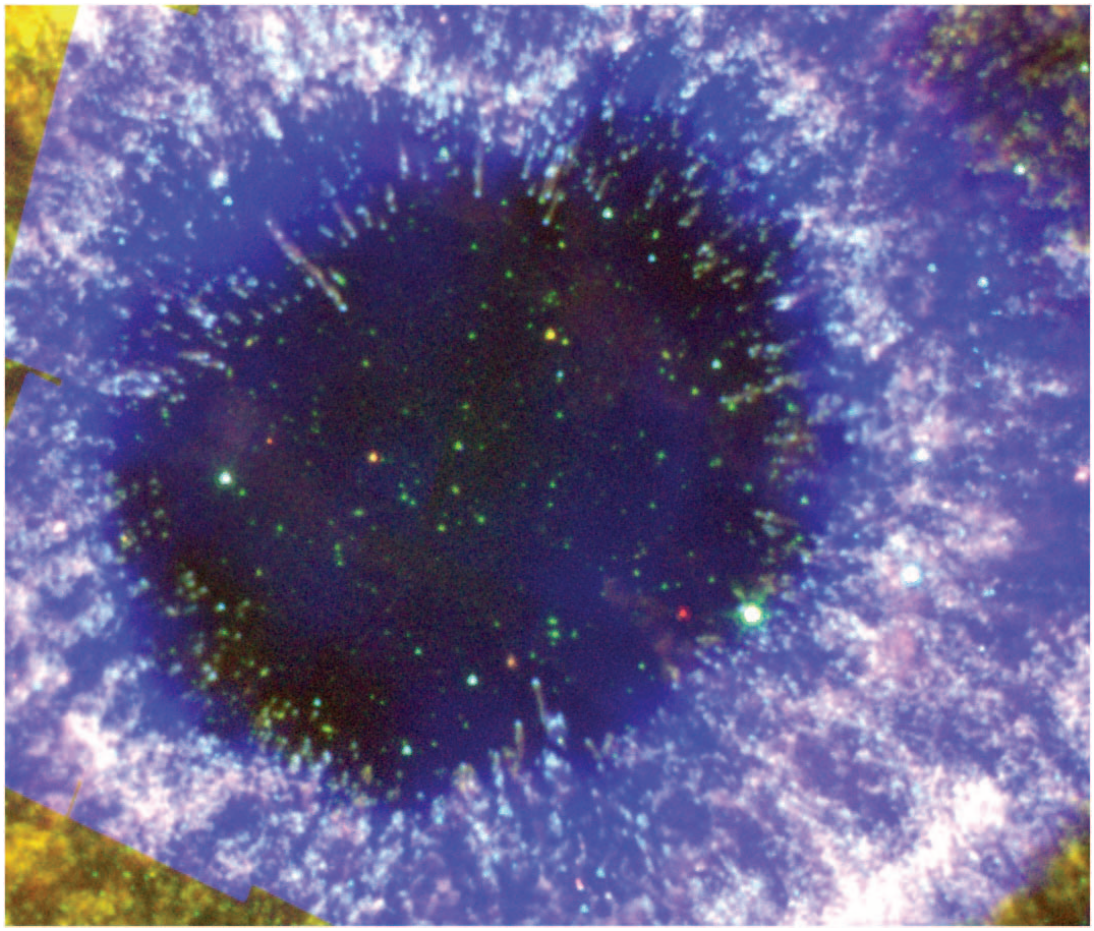

FIG. 7.—Three-color image of the central region of the Helix. The IRAC 8 μm image is red, 4.5 μm is green, and the ACS F658N image (Hα + [N II]) is blue. The ACS image was smoothed to match the resolution of the IRAC images. The ACS image does not completely cover the field, which is evident in the corners of this image.

et al. 1990). The absence of any detectable lines from the higher vibrational states in our IRS spectra, in particular the normally strong 1–1 $S(7)$ line, is convincing evidence that the emission is thoroughly dominated by shocks, although from our limit on the 1–1 $S(7)$ line we cannot exclude a modest contribution from PDRs at a level below about 10% of the shock contribution. We therefore have modeled the emission by relying completely on C-type shock excitation and have done so successfully. We are able to fit the observed IRS line strengths to better than a few percent with a combination of three shocks with velocities of 20, 35, and $\sim$5 km s^{-1}. The dominant shock has a velocity of 20 km s^{-1}, with 75% of the strongest feature [the 0–0 $S(5)$ line] being produced in this shock. A 20 km s^{-1} shock is unable to explain the relative strengths of the more highly excited 0–0 $S(7)$ or 0–0 $S(6)$ lines, and an additional component with $v = 35$ km s^{-1} was required to boost these lines. This faster shock provides about 25% of the observed flux of the fiducial 0–0 $S(5)$ line.

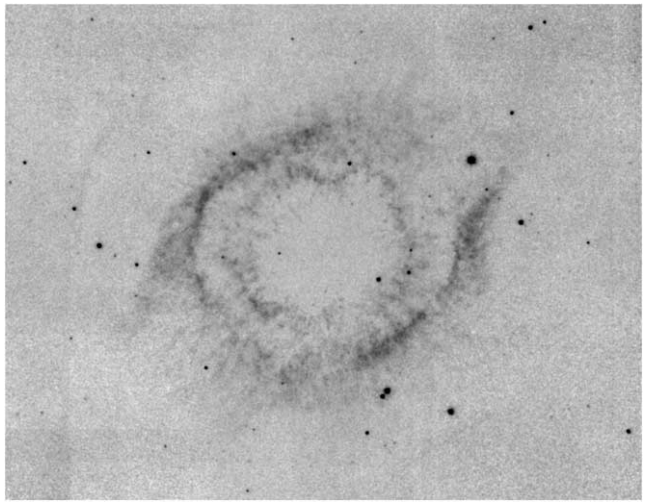

FIG. 8.—Narrowband H_2 (2.12 μm) image of the Helix obtained with QUIST. North is up, and the image is approximately $29' \times 23'$.

The 0–0 $S(1)$ line at 17 μm is considerably stronger than predicted by the combination of these two shocks, but because it is so easily excited (its upper state is at 171 K) any modest shock with $v \sim 5$ km s^{-1} can excite this line without producing significant amounts of other line emission; in our best model 66% of the 0–0 $S(1)$ line comes from such a very slow shock, which contributes less than a few percent to the other lines. We found that for the higher velocity shock cases a preshock density of $n = 1 \times 10^5$ cm^{-3} consistently gave a marginally better fit than did any other density, and we adopted it throughout; both lower densities tended to produce an overintensity of 0–0 $S(3)$ emission. For the slow shock component, the density was not a sensitive indicator. There is one additional line we can use in our modeling, the 1–0 $S(1)$ line at 2.12 μm. Our best, three-velocity component shock model contributes only 1×10^{-20} W cm^{-2} to

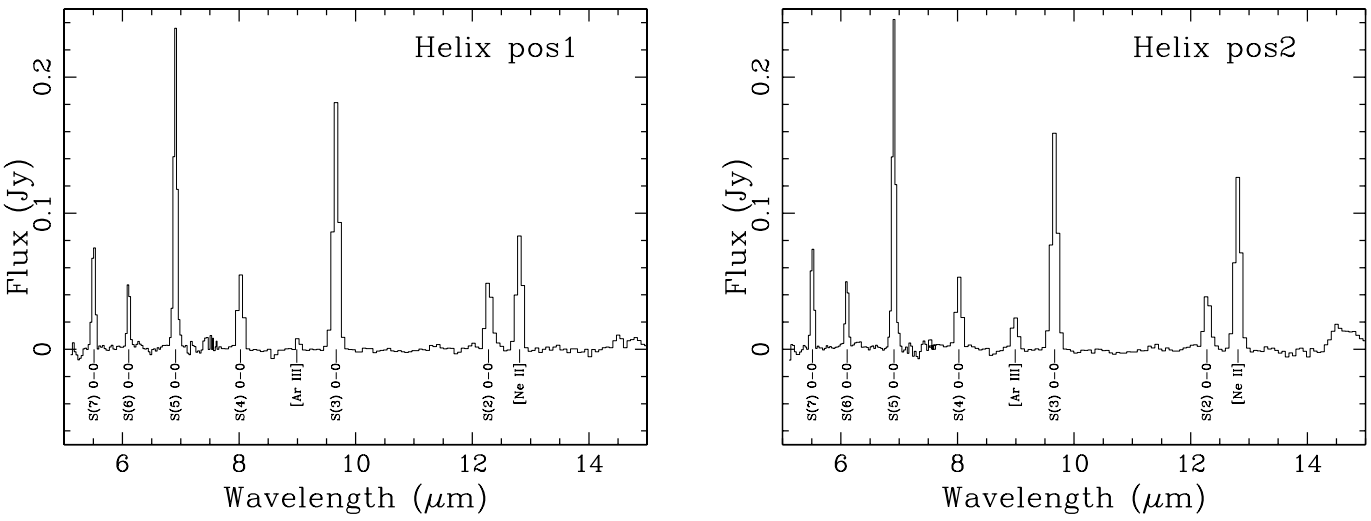

FIG. 9.—IRS spectra of the two positions in the Helix (see Fig. 10). The spectra from the "IRS OFF" position was subtracted before extracting these spectra.

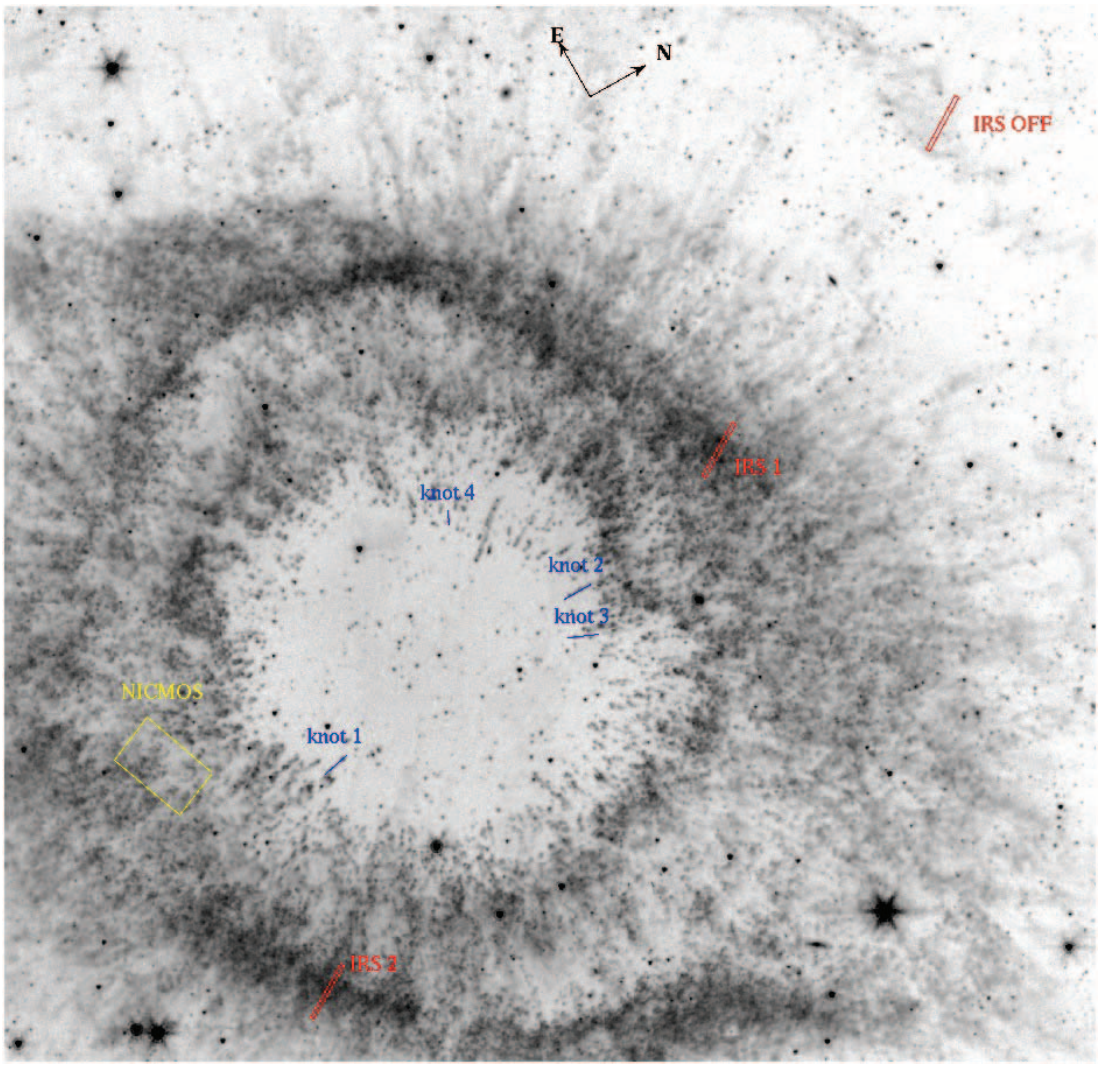

FIG. 10.—Locations of the IRS slits and the knots that are discussed in the text, plotted on the IRAC 4.5 μm image.

TABLE 2
LINE FLUXES FROM THE IRS SPECTRA

Line ID	Wavelength (μm)	Position 1 (10^{-20} W cm^{-2})	Position 2 (10^{-20} W cm^{-2})
H_2 (0, 0) $S(7)$	5.51116	5.85	5.15
H_2 (0, 0) $S(6)$	6.10856	2.44	2.73
H_2 (0, 0) $S(5)$	6.90952	10.4	10.5
H_2 (0, 0) $S(4)$	8.02505	3.08	2.91
[Ar III]	8.99138	0.29	1.37
H_2 (0, 0) $S(3)$	9.66491	7.45	6.77
H_2 (0, 0) $S(2)$	12.2786	1.37	1.15
[Ne II]	12.8135	2.01	3.17
H_2 (0, 0) $S(1)$	17.0348	2.38	...

this line. From the ground-based image in the 1–0 $S(1)$ line at 2.12 μm in Figure 8, we estimated the flux in this line in the $3\farcs6 \times 57''$ region of the IRS slit is 2×10^{-20} W cm^{-2}, considerably more than we can account for with this scenario. However, a PDR contribution could be fully consistent with this measured flux. The limit to a PDR contribution from the limit in our IRS data, to the 1–1 $S(7)$ line, is less than about 10% of the shock contribution. A PDR with density of $n = 1 \times 10^3$ (insensitive to the local UV field) that contributes less than about 5% to the pure rotational lines gives a 1–0 $S(1)$ flux of 1.2×10^{-20} W cm^{-2}. When this is added to the shock contribution, it can explain the observed emission as measured in the 2.12 μm image. We emphasize that while our model uses a three-component shock and rejects parameters that are significantly different, it is of course most probable that a wide range of shocks are present and our model simply fits them all to these parameters. Sternberg & Dalgarno (1995) have examined cases with very dense (10^6 cm^{-3}) high-UV-excited ($G = 2 \times 10^5$) gas, but this density is unrealistically more than even the highest density estimate of Meixner et al. (2005) of 10^4–10^5 cm^{-3} for the small knots in the Helix and is inappropriate in the Helix case.

The measured fluxes in the lines enable us to estimate the filling factor for the shock in the IRS $3\farcs6 \times 57''$ beam. The dominant 20 km s^{-1} component has a filling factor of about 1.3×10^{-3}, while the 35 km s^{-1} shock has a smaller factor of 7.4×10^{-5}. The total luminosity in all the hydrogen lines, from the combined best model, is 3×10^{-3} $L_\odot$ from this region of the Helix, 60% of which is from the 20 km s^{-1} component. Our IRAC band 3 flux in this IRS region is about 3 mJy; the total IRAC band 3 flux for the entire Helix is about 1000 times greater, about 3 Jy. If the shock is everywhere similar to the region we have mapped, then the total H_2 line flux from the Helix can be scaled accordingly, for a total value of about 3 $L_\odot$, about 5% of the total luminosity of the Helix. This number is consistent with estimates from other authors as well (e.g., Cox et al. 1998). Together with our estimates for the filling factor and scaling with luminosity for the entire nebula as above, these numbers imply a total mass in excited H_2 of a few Earth masses.

TABLE 3
IRAC FLUXES IN THE IRS SPECTRA POSITIONS

Band	Position 1 (mJy)	Position 2 (mJy)
IRS 5.8 μm	6.2	6.0
IRS 8 μm	8.3	8.2
Ratio $F_{5.8\,\mu m}/F_{8\,\mu m}$	0.76	0.59
IRAC 3.6 μm	1.5	1.7
IRAC 4.5 μm	2.8	3.2
IRAC 5.8 μm	5.9	6.0
IRAC 8 μm	7.8	7.6
Ratio $F_{5.8\,\mu m}/F_{8\,\mu m}$	0.76	0.78

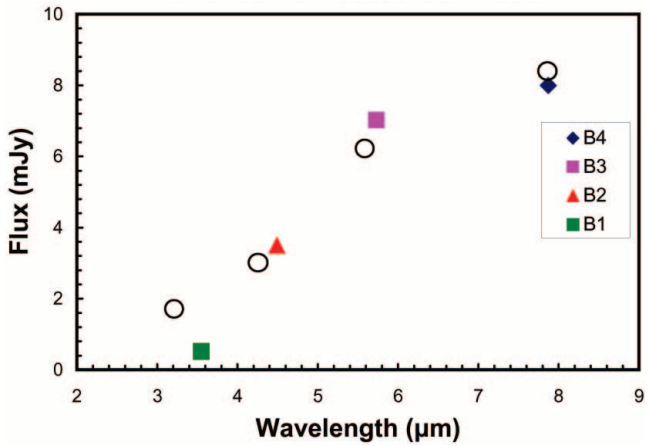

FIG. 11.—IRAC fluxes from best shock model. The colored symbols are the predicted contribution to the IRAC band fluxes from H_2 line emission in the IRS slit region. The circles are the measured IRAC flux densities summed over the IRS slit.

From the best-fit model we are able to calculate the corresponding fluxes in the IRAC bands by converting each of the observed line strengths into a flux density in the appropriate IRAC band using the IRAC instrumental response procedures as described in § 5.2 of the IRAC Data Handbook and as also described in Smith et al. (2006; they note that ver. 2.0 of the handbook contains some significant errors in the "Photometry and Calibration" section). We have used the corrected handbook values (W. Reach 2006, private communication).

Figure 11 shows the net predicted contribution to the IRAC band fluxes from H_2 line emission in the IRS slit region; the circles are the measured IRAC flux densities summed over the IRS slit. Table 4 shows the model fluxes from H_2 lines in IRAC bands 1 and 2. The results confirm a result noted by Smith et al. (2006) regarding the shock in DR 21, namely, that in shocks the H_2 lines contribute significantly to the IRAC band fluxes. Smith et al. (2006) also report that in the shocked outflow of DR 21, PAH emission (at either 6.2 or 7.7 μm) is absent. The Helix is even more dramatic than DR 21 in that our spectra show a very low continuum level consistent with zero at a level of about 3×10^{-20} W cm^{-2}. Cohen & Barlow (2005) found PAH emission in 17 of 43 PNs they studied with *ISO* and concluded that as a general rule when the C/O ratio was less than about 0.6 there was no PAH emission; they do report, however, the exception of NGC 6720, which has a C/O ratio of 0.62 yet no detected PAH emission. Our nondetection of PAH emission in the Helix is consistent with the broad trends that Cohen & Barlow report. As a result, the H_2 lines (as seen in Fig. 11) contribute more than 90% of the flux in IRAC bands 2, 3, and 4.

Our limited spectral data on the Helix do not allow us to determine the reason for the absence of PAH emission here. In the case of the DR 21 outflow, the possibilities considered for the absence of PAHs were shock or UV depletion of the material or the absence of a suitable PDR environment. Cox et al. (1998) studied the Helix and its H_2 lines with the ISOCAM circular variable filter (CVF); they also conclude that PDR excitation in the Helix is inadequate to explain the H_2 lines they measured. They consider C- and J-type shocks but argue

TABLE 4
MOLECULAR HYDROGEN MODEL FLUXES IN IRAC BANDS 1 AND 2

Line ID	Wavelength (μm)	Flux Density (mJy)
Band 1 (3.6 μm)		
2–1 *O*(9)	4.884	...
0–0 *S*(9)	4.694	0.52
1–0 *O*(9)	4.576	...
2–1 *O*(8)	4.438	...
0–0 *S*(10)	4.410	0.012
0–0 *S*(11)	4.181	...
1–0 *O*(8)	4.163	...
2–1 *O*(7)	4.054	...
0–0 *S*(12)	3.996	...
Total:	...	0.54
Band 2 (4.5 μm)		
0–0 *S*(13)	3.846	...
1–0 *O*(7)	3.807	0.058
2–1 *O*(6)	3.724	...
0–0 *S*(14)	3.724	...
0–0 *S*(15)	3.626	...
0–0 *S*(16)	3.547	...
1–0 *O*(6)	3.501	0.053
0–0 *S*(17)	3.485	...
0–0 *S*(18)	3.438	...
2–1 *O*(5)	3.438	...
1–0 *O*(5)	3.235	0.31
2–1 *O*(4)	3.190	...
Total	...	0.42

that neither of these scenarios offers a convincing answer, C-type shocks because of the weak magnetic fields thought to be present in the in the Helix and nondissociative J-type shocks because they require lower densities and/or temperature than are inferred. Finally, they note that there is no strong evidence in the Helix for a stellar wind capable of generating such shocks. The fact that the Kaufmann, Wolfire, and Hollenbach shock models fit so precisely our observed line fluxes, at least in the combination we describe above, suggests to us that we must reexamine all of these assumptions about conditions in the Helix Nebula. In particular, our data indicate that there are (or were) strong winds (or other shock-producing mechanisms) present in this planetary nebula and furthermore that there is enough magnetic field in the outer shell to prevent the higher velocity shocks from dissociating the molecules. High-velocity gas is well known to exist in the Helix. Young et al. (1999) mapped the molecular envelope in CO 2–1 and report gas motions of more than 50 km s^{-1}, more than adequate to shock the H_2 in our models. In their study of the origin and nature of the Helix structure, they conclude that there is evidence for directed bipolar flow in the early stages of development of the Helix, and that or related activity could produce the shocks we apparently see in H_2.

4.2. *Variation of the* H_2 *Emission in the Knots and Nebula*

As noted above, the relative strength of the emission in the IRAC bands varies as a function of distance from the central star and on small scales as in the cometary knot tips and the inner edges of the structures in the ring. Our IRS spectra only cover a tiny portion of the nebulosity, and these locations were chosen because of the bright knots known to be there; therefore, some caution should be exercised when extrapolating our spectral conclusions to the entire region. Nevertheless, *HST* and radio studies do not find any evidence that the area of our spectral study is dramatically different in kind from other spots in the Helix, and it is useful to see if a consistent picture can emerge from the IRAC images alone with this proviso. As shown in Figure 5, the tips of the knots have the highest 4.5 μm/8.0 μm emission ratio, and the value in the main ring and outward decreases as the radius increases. The 3.6 μm/4.5 μm ratio remains relatively constant over the same radius range, increasing only slightly at higher radius. The H_2 models indicate that this trend can be matched by a decreasing shock velocity and density as the radius increases. The small-scale color differences could be a result of a higher PDR contribution to the H_2 emission on the inner edges of the clumps.

5. COMETARY KNOTS AND CLUMPS

5.1. *Enhanced Structure Images*

In order to show the small-scale structure more clearly, we processed the IRAC images by dividing the image by a median-smoothed version of the same image using a square kernel of 20.″4 in size, similar to what was done by O'Dell et al. (2004) for their [O III] image. The results are shown in Figures 12–17. Figures 12 and 13 show the processed 4.5 and 8 μm images, and Figures 14 and 15 show the inner $10' \times 9'$ region. Outside the innermost region, the appearance of the nebula is clumpy on small scales, lacking the long tails of the cometary knots of the inner region. The size and structure of the clumps is fairly uniform across the nebula, and the long radial rays are seen only in the outer regions, outside the main ring. The images show that the H_2 structure observed in the NICMOS images of Meixner et al. (2005) in Figure 6 are representative of most of the main ring region.

Color versions of the enhanced structure images are shown in Figures 16 and 17. Figure 16 is a three-color image of the 8, 4.5, and 3.6 μm IRAC enhanced structure images mapped to red, green, and blue, respectively. The color difference between the inner blue-green region of the cometary knots and the outer redder clumps is visible here.

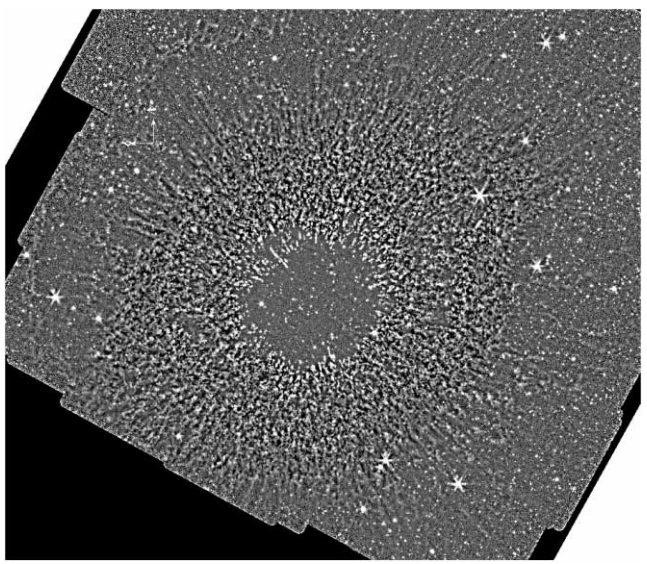

FIG. 12.—IRAC 4.5 μm image with the small-scale structure enhanced by taking the ratio of the original image to its local median, as described in § 4.1. North is at the top, and the field shown is approximately $45' \times 23'$.

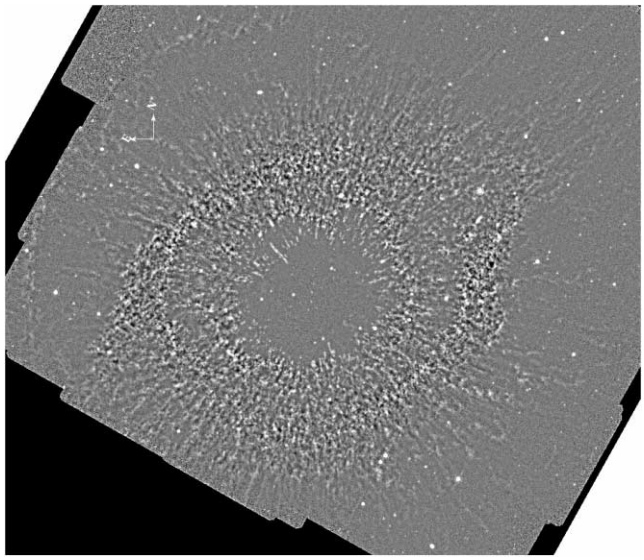

FIG. 13.—Same as Fig. 12, but for the 8 μm image.

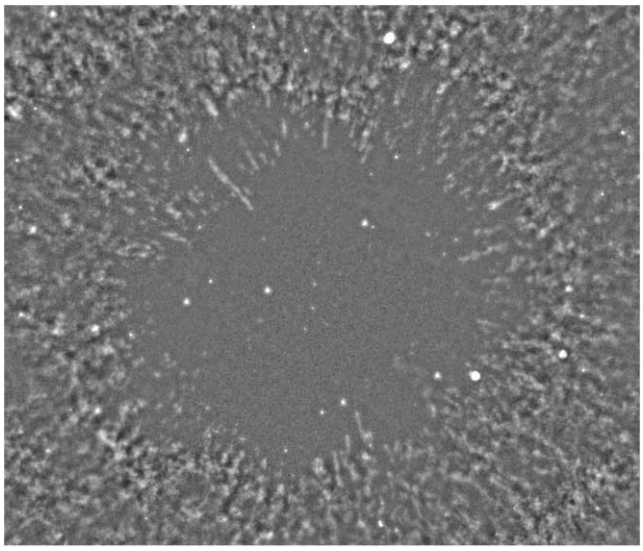

FIG. 15.—Same as Fig. 13, but showing the inner $10' \times 9'$ region.

Figure 17 shows the IRAC 8 and 4.5 μm images mapped to red and green, respectively, and the ACS F658N image mapped to blue. The structure-enhanced versions of the images were used. Two important characteristics of the emission are shown in this image. First, as seen before, the color structure of the cometary knots are readily visible, with their blue-green tips and red tails. This image also shows that there are bright blue emission regions in many of the locations where there is a minimum of IRAC emission. This is a result of the different sources of the emission in these bands: the emission in the ACS F658N filter is primarily from the Hα and [N II] lines in the ionized regions of the nebula, whereas the IRAC structure is primarily from the H_2 lines at the interface between the ionized regions and the molecular material. This shows that the two emission components are fairly well mixed on larger spatial scales, but on smaller scales the emission is spatially segregated. The H_2 has a clumpy distribution, and the emission from the ionized gas is strongest in the voids between the clumps. This is consistent with the gas being either not present near the H_2 clumps or shielded from the ionizing radiation from the central star in the shadow of the clumps.

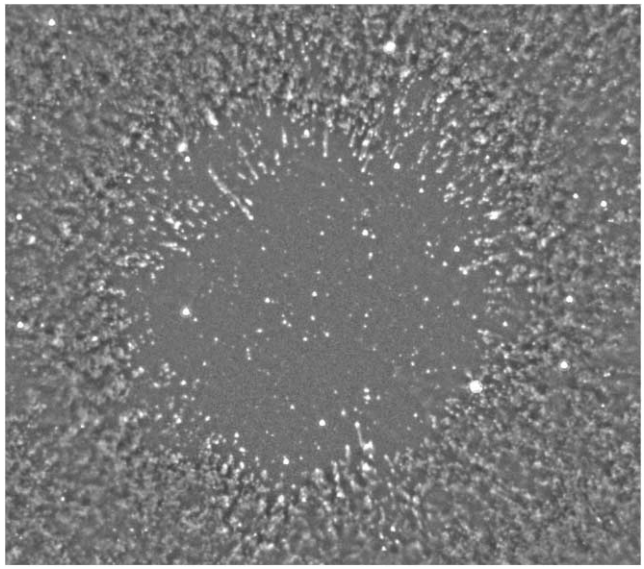

FIG. 14.—Same as Fig. 12, but showing the inner $10' \times 9'$ region.

5.2. *Structure of the Knots*

Figure 18 shows profiles of the emission through four cometary knots. The knots examined are indicated in Figure 10, and the identifications and positions are given in Table 5. The profile width was 2″. The 0.658 μm (Hα + [N II]) image was convolved with a Gaussian to match the spatial resolution of the IRAC images. The 0.658 μm emission peak appears at the inner edge of the knots, and IRAC bands 1, 2, and 4 peak about an arcsecond or more behind the optical line emission in each case. The emission drops off rapidly in all bands except for the 8 μm band, which drops off to a plateau that extends the length of the tail. The IRAC 3.6 and 4.5 μm bands drop off slightly less than the optical emission but roughly follow the 0.658 μm profile.

The structure of the H_2 emission in the cometary knots in the IRAC images differs from that in Walsh & Ageorges (2003), who report that in their 2.12 μm imaging of the cometary knots with 1.″2 seeing the H_2 emission is seen only in the low-ionization region facing the central star but not in the cores of the knots. They do note that H_2 was seen in some of the tails. With IRAC, the H_2 emission is seen all along the knot, although with IRAC's resolution, the emission from the rim of the knot would fill in the neutral core and we would not resolve an emission-free region. However, the spatial distribution of the 2.12 μm emission reported by Walsh & Ageorges (2003) is consistent with the trend seen in the IRAC data, in which at shorter wavelengths, more of the emission is concentrated in the tip of the knot and less along the length of the cometary tail.

5.3. *Number of Knots*

There have been several estimates of the number of knots in the Helix, with Meixner et al. (2005) recently updating the estimate based on their NICMOS observations. They counted the number of knots in the field of view and assumed the same statistics over the area of the main ring, concluding that there are a total of ~23,000 knots. Because we have imaged the entire ring

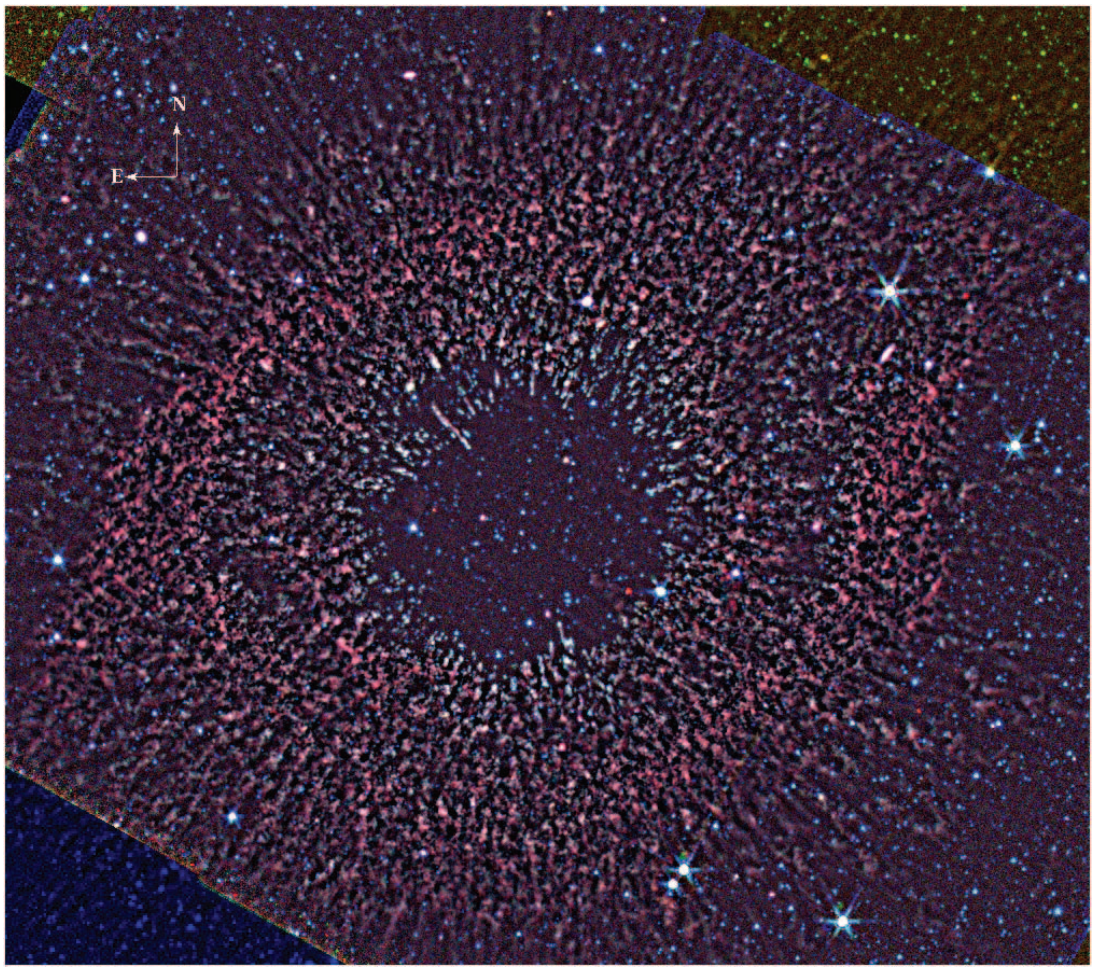

FIG. 16.—IRAC three-color image (the 8, 4.5, and 3.6 μm images mapped to red, green, and blue, respectively) using the structure-enhanced images as described in § 4.1.

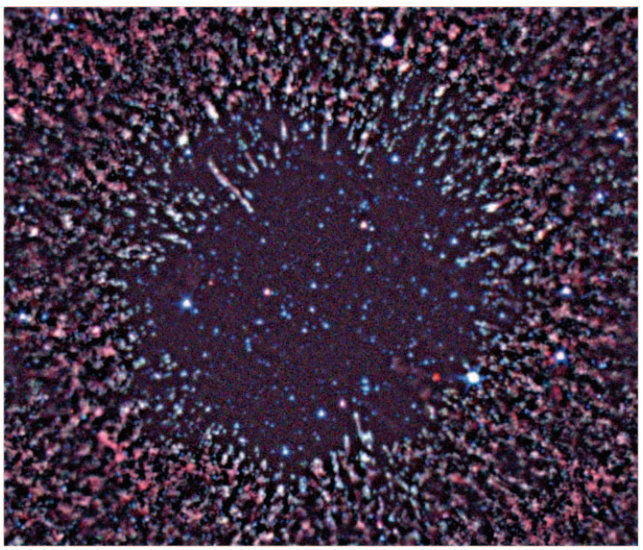

FIG. 17.—Three-color image (the 8 and 4.5 μm IRAC images and the ACS F658N image mapped to red, green, and blue, respectively) of the central region of the Helix. This image used the structure-enhanced versions of the images as described in § 4.1.

with IRAC, we can more directly estimate the number of knots without extrapolating. We used the IRAC 8 μm image for the estimate because it is the least sensitive to optical depth through the nebula and provides the most accurate total flux from the knots. Due to the limited resolution and large number of overlapping knots in the main ring, it is impossible to individually count the knots from the image. The number of knots can be estimated by determining the average flux from one knot and then dividing the total flux by the average to obtain the number of knots. We examined individual knots inside the main ring to determine the average flux. The *HST* ACS image was used to identify the knots and their boundaries, and the average fluxes for a sample of 30 knots were determined. The area used for the average included the bright heads of the knots as well as emission from the fainter tails. The knot fluxes varied over a factor of 2 (from $\sim$240 to $\sim$480 μJy per knot), resulting in an estimate of 20,000–40,000 knots in the main ring. Adding to the uncertainty is the fact that the appearance of the knots changes as a function of radius. If the change is not just an evolution of the morphology but a change in the total H_2 emission as a result of different mass or excitation, then this estimate of the number of knots would be affected.

We cannot directly estimate the total mass of the knots, since the H_2 emission detected by IRAC is from the surface of the knots and comprises a relatively small fraction of the mass. Meaburn et al. (1992), O'Dell & Handron (1996), and Huggins

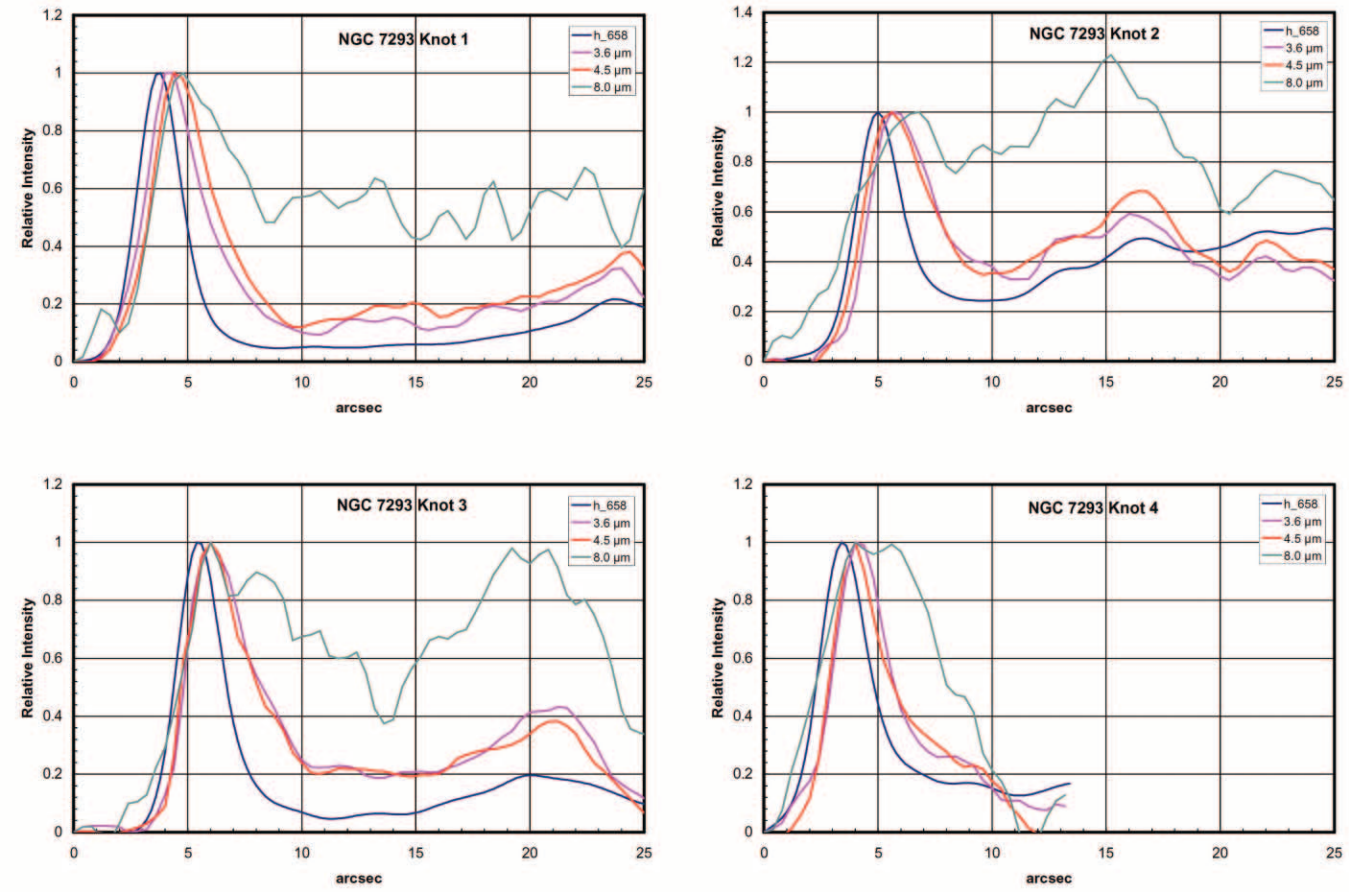

FIG. 18.—Plots showing the profiles of the emission through each of four separate knots. In each plot, the knot profiles from the 0.658, 3.6, 4.5, and 8 μm images are shown. The profile was extracted along a vector aligned in the radial direction, plotted in the inner to outer direction (see Fig. 10 and Table 5 for the location of the knots). The width of the extracted region was 2″.

et al. (2002) estimate the total mass of the knots in the range of $(1–2) \times 10^{-5}\ M_{\odot}$. Adopting a mass of 1.5×10^{-5} would result in a total mass of the knots in the range of $0.3–0.6\ M_{\odot}$. This is comparable to the total ionized mass estimated by Henry et al. (1999) of $0.3\ M_{\odot}$ and in agreement with the result of Meixner et al. (2005).

6. HALO STRUCTURES

Outside the main rings, the character of the emission changes. The images in Figures 1, 12, and 17 show that the region between the main ring and the northeast arc (hereafter NE arc, in the nomenclature of O'Dell et al. 2004) is filled with long radial rays and large arc-shaped structures, in contrast to the main ring, where the compact knots dominate. The rays in the halo also differ from the cometary knots in that they do not have bright inward-facing tips, and the features in the halo are much broader. The emission extends to the edges of the IRAC images, beyond the shell of which the NE arc is the brightest feature. In the 5.8 and 8 μm images in particular, one can see the rays extending beyond the NE arc ring in the east and north. In the eastern corner of the

TABLE 5
NGC 7293 KNOTS AND PROFILE POSITIONS

		START (J2000.0)		END (J2000.0)	
KNOT NUMBER	NAME[a]	R.A.	Decl.	R.A.	Decl.
1	356-216	22 29 35.76	−20 52 12.9	22 29 35.20	−20 52 35.5
2	378-800	22 29 37.79	−20 48 06.7	22 29 37.79	−20 48 38.2
3	352-815	22 29 35.40	−20 48 18.9	22 29 34.40	−20 47 54.5
4	459-905	22 29 45.75	−20 49 07.6	22 29 46.60	−20 49 35.0

NOTES.—Units of right ascension are hours, minutes, and seconds, and units of declination are degrees, arcminutes, and arcseconds. The positions show the start and stop coordinates of the profiles shown in Fig. 18. The profile width is 2″.

[a] The knot ID in the scheme of O'Dell & Burkert (1997), which is based on the position of the bright head of the knot. The first number is the tenths of the right ascension seconds coordinate, and the second number is the last digit of the declination coordinate's minutes appended to the declination seconds.

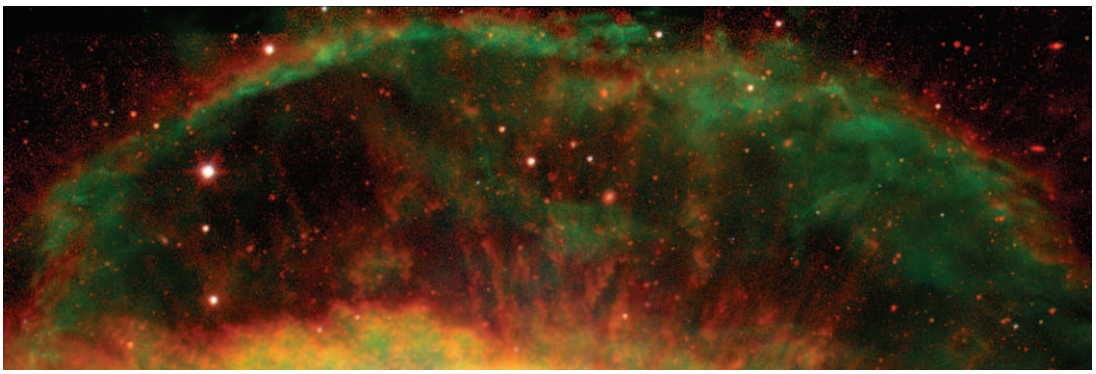

FIG. 19.—Combined *Spitzer* (4.5 and 8 μm), Hα + [N II], and [O III] images (O'Dell et al. 2004) shown as red, green, and blue, respectively. North is 60.°9 clockwise from up. The image shows clearly that the H_2 emission is located in a shell just outside the Hα emission.

5.8 μm image, a rim of another outer shell seems to be visible about where the southeast plume terminates. We have planned further IRAC observations to determine the extent of this outer halo.

6.1. *Northeast Arc*

Figure 19 shows a comparison between the infrared and optical emission of the NE arc.[4] In this color image, green is the Hα + [N II] image from O'Dell et al. (2004), and red is an average of the IRAC 4.5 and 8 μm bands. The characteristics of the emission are similar in the optical and infrared, except that the IR emission, primarily from H_2, is located in a shell adjacent to and outside the optical emission. The structure of the shell differs greatly from the main ring, which is about half as far from the central star. Instead of being very clumpy, at or below the resolution of the IR images, the features in the arc are more extended, with a minimum width or size of 10″. The emission is in a relatively thin shell, compared to the main rings, which are radially thicker. The morphology of the arc and the relative locations of the Hα and molecular emission suggest that this arc is a PDR viewed nearly edge-on.

The separation of the ionized gas and H_2 emission in the NE arc is markedly different from in the main ring. In the ring, the clumps of emission seem to coexist with the ionized gas. What structure that exists in the Hα emission seems to be anticorrelated with the H_2 clumps but not segregated radially. It is difficult to envision a scenario in which complicated structures such as those in the main ring and cometary knots could evolve to a simpler shell structure such as that in the NE arc. Therefore, it would seem that the mass ejection episode that created the main rings was quite different from the episode that created the outer shell. There are several examples of other PNs that also have more spherically symmetric or simpler outer halos but complicated inner structures. For example, NGC 6720 has a clumpy asymmetric inner main ring surrounded by a nearly circular outer arc (Speck et al. 2002). NGC 6543 has a complicated inner structure surrounded by spherical shells (Mitchell et al. 2005).

6.2. *Radial Rays*

The region between the main ring and the outermost arcs is filled with small arcs and radial rays. These features are visible in all of the bands but are most pronounced in the 5.8 and 8 μm images in Figure 3. Some of the small arcs could be parts of the same shell as the NE arc seen in projection on the sky at smaller radial distances. However, the rays seem to be different in character, with their long dimension oriented radially from the central star and extending from the main rings to the outer arcs and beyond.

The rays are also visible in optical images. The [O III] images of O'Dell et al. (2004) show rays as well (their Figs. 13 and 16) but primarily in and just outside the main ring. The rays are not as visible in the main ring in the IRAC images, in part because of the greater number of emission clumps in the IR data. Outside the main ring, the rays are visible in the IRAC data but the brightness in [O III] drops rapidly. Where the IR and optical rays overlap, there is little or no correspondence to the positions of the optical and IR rays; in fact, they seem to be if anything anticorrelated. This implies that the IR rays are in the shadow of clumps in the main ring, and the optical rays are where the light from the central star shines through holes between the clumps. However, it is difficult to trace the rays to any one clump or group of clumps because of their density; if one traces a line inward from the IR ray, the line passes through many clumps.

Recent optical imaging by Meaburn et al. (2005) in the Hα + [N II] lines shows faint radial rays in the inner region, at smaller radii than for the cometary knots. The IRAC images do not show any trace of these structures; the inner region has only faint diffuse emission that is on the order of 1′ in size. These could be wisps of halo emission that are in front of or behind the main nebula and seen in projection close to the central star.

7. CONCLUSIONS

We have presented IRAC images and IRS spectra of the Helix PN. The emission from the nebula is dominated by the pure rotational lines of H_2 with a smaller contribution from forbidden line emission such as [Ar III] in the ionized region. The H_2 emission is consistent with models of shock excitation, with an approximately 10% contribution from H_2 excited in PDRs. No evidence of PAH emission is seen in the spectra, which might have been expected based on its nebular C/O ratio.

The emission in the nebula is concentrated in small knots and clumps throughout the main rings. There is an anticorrelation between the H_2 emission and the ionized gas as traced by Hα images, indicating a segregation of the molecular and ionized gas on the scale of the observed clumps. The IRAC images resolve the extensively studied cometary knots in the inner region of the nebula. The tails of the knots and the radial rays extending into the outer regions of the PN are seen in emission in the IRAC

[4] The full image is available at http://www.spitzer.caltech.edu/Media/releases/ssc2006-01/ssc2006-01b.shtml.

bands. In the northeast arc, the H_2 emission is located in a shell outside the Hα emission.

We gratefully thank Mark Wolfire and Michael Kaufman for providing us with their latest calculations of the H_2 line strengths. We thank M. S. Kelley for providing his IRS extended source correction to us. This work is based in part on the IRAC post-BCD processing software IRAC_proc developed by Michael Schuster, Massimo Marengo, and Brian Patten at the Smithsonian Astrophysical Observatory. This work is based in part on observations made with the *Spitzer Space Telescope*, which is operated by the Jet Propulsion Laboratory, California Institute of Technology under NASA contract 1407. Support for this work was provided by NASA through contract 1256790 issued by JPL/Caltech. Support for the IRAC instrument was provided by NASA through contract 960541 issued by JPL. This work made use of the Two Micron All Sky Survey (2MASS) database, which is a joint project of the University of Massachusetts and the Infrared Processing and Analysis Center/California Institute of Technology, funded by the National Aeronautics and Space Administration and the National Science Foundation. H. A. S. acknowledges partial support from NASA grant NAG5-10654.

Facilities: Spitzer

REFERENCES

Aitken, D. K., & Roche, P. F. 1983, MNRAS, 202, 1233
Black, J. H., & van Dishoeck, E. F. 1987, ApJ, 322, 412
Bunn, J. C., Hoare, M. G., & Drew, J. E. 1995, MNRAS, 272, 346
Cohen, M., & Barlow, M. J. 2005, MNRAS, 362, 1199
Cox, P., et al. 1998, ApJ, 495, L23
Fazio, G. G., et al. 2004, ApJS, 154, 10
Harris, H. C., Dahn, C. C., Monet, D. G., & Pier, J. R. 1997, in IAU Symp. 180, Planetary Nebulae, ed. H. J. Habing & H. J. G. L. M. Lamers (Dordrecht: Kluwer), 40
Henry, R. B. C., Kwitter, K. B., & Dufour, R. J. 1999, ApJ, 517, 782
Hodapp, K.-W., et al. 1996, NewA, 1, 177
Hora, J. L., Deutsch, L. K., Hoffmann, W. F., Fazio, G. G., & Shivanandan, K. 1993, ApJ, 413, 304
Hora, J. L., Latter, W. B., Allen, L. E., Marengo, M., Deutsch, L. K., & Pipher, J. L. 2004a, ApJS, 154, 296
Hora, J. L., Latter, W. B., Marengo, M., Fazio, G. G., Allen, L. E., & Pipher, J. L. 2005, BAAS, 37, 493
Hora, J. L., et al. 2004b, Proc. SPIE, 5487, 77
Houck, J. R., et al. 2004, ApJS, 154, 18
Huggins, P. J., Bachiller, R., Cox, P., & Forveille, T. 1992, ApJ, 401, L43
Huggins, P. J., Forveille, T., Bachiller, R., Cox, P., Ageorges, N., & Walsh, J. R. 2002, ApJ, 573, L55
Kaufman, M. J., Hollenbach, D. J., Bergin, E. A., Melnick, G. J., Snell, R. L., Li, D., & Walmsley, C. M. 2005, in IAU Symp. 231, Astrochemistry Throughout the Universe, ed. D. C. Lis, G. A. Blake, & E. Herbst (Cambridge: Cambridge Univ. Press), 179
Kaufman, M. J., & Neufeld, D. A. 1996, ApJ, 456, 250
Kaufman, M. J., Wolfire, M. G., & Hollenbach, D. J. 2006, ApJ, 644, 283
Kelley, M. S., Woodward, C. E., Harker, D. E., Reach, W. T., & Gehrz, R. D. 2005, BAAS, 37, 1156
Meaburn, J., Boumis, P., López, J. A., Harman, D. J., Bryce, M., Redman, M. P., & Mavromatakis, F. 2005, MNRAS, 360, 963
Meaburn, J., Walsh, J. R., Clegg, R. E. S., Walton, N. A., & Taylor, D. 1992, MNRAS, 255, 177
Meixner, M., McCullough, P., Hartman, J., Son, M., & Speck, A. 2005, AJ, 130, 1784
Mitchell, D. L., et al. 2005, MNRAS, 362, 1286
O'Dell, C. R., & Burkert, A. 1997, in IAU Symp. 180, Planetary Nebulae, ed. H. J. Habing & H. J. G. L. M. Lamers (Dordrecht: Kluwer), 332
O'Dell, C. R., & Handron, K. D. 1996, AJ, 111, 1630
O'Dell, C. R., Henney, W. J., & Ferland, G. J. 2005, AJ, 130, 172
O'Dell, C. R., McCullough, P. R., & Meixner, M. 2004, AJ, 128, 2339
Reach, W. T., et al. 2005, PASP, 117, 978
Schuster, M. T., Marengo, M., & Patten, B. 2006, Proc. SPIE, 6270, 65
Smith, H. A., Hora, J. L., Marengo, M., & Pipher, J. L. 2006, ApJ, 645, 1264
Speck, A. K., Meixner, M., Fong, D., McCullough, P. R., Moser, D. E., & Ueta, T. 2002, AJ, 123, 346
Sternberg, A., & Dalgarno, A. 1995, ApJS, 99, 565
Walsh, J. R., & Ageorges, N. 2003, in IAU Symp. 209, Planetary Nebulae: Their Evolution and Role in the Universe, ed. S. Kwok, M. Dopita, & R. Sutherland (San Francisco: ASP), 275
Werner, M., et al. 2004, ApJS, 154, 1
Wolfire, M. G., Tielens, A. G. G. M., & Hollenbach, D. 1990, ApJ, 358, 116
Young, K., Cox, P., Huggins, P. J., Forveille, T., & Bachiller, R. 1999, ApJ, 522, 387